RESEARCH ARTICLE

Key Points:
- Injection-induced fault slip plausible for Timpson M_w4.8 earthquake sequence
- Fault reactivation potential sensitive to fault orientation, stress state, and reservoir permeability
- Low fault and reservoir permeabilities favor fault reactivation

Geomechanical analysis of fluid injection and seismic fault slip for the M_w4.8 Timpson, Texas, earthquake sequence

Zhiqiang Fan[1], Peter Eichhubl[1], and Julia F. W. Gale[1]

[1]Bureau of Economic Geology, Jackson School of Geosciences, The University of Texas at Austin, Austin, Texas, USA

Abstract An earthquake sequence that culminated in a M_w4.8 strike-slip event near Timpson, east Texas, the largest reported earthquake to date in that region, had previously been attributed to wastewater injection starting 17 months before the onset of recorded seismic activity. To test if this earthquake sequence can be attributed to wastewater injection, we conducted coupled poroelastic finite element simulations to assess the spatial and temporal evolution of pore pressure and stress field in the vicinity of the injection wells and to calculate the Coulomb failure stress on the seismogenic fault as a function of the permeability of the injection layer, fault orientation, fault permeability, and orientation and magnitude of the in situ stress. We find that injection-induced fault slip is plausible within the range of selected model input parameters, with slip favored by low reservoir permeability, low fault permeability, and a favorable orientation of the fault relative to the in situ stress state. Other combinations of equally plausible input parameters predict no slip within 96 months of simulated injection. Under most favorable boundary conditions for fault slip, fault slip occurs 7 months after the start of injection. Our results highlight the importance of detailed geomechanical site characterization for robust fault stability assessment prior to wastewater injection.

1. Introduction

Injection of wastewater including formation water coproduced with oil and gas from hydrocarbon reservoirs and flow back after hydraulic fracturing of tight unconventional reservoirs is routinely practiced on a large commercial scale. In some occurrences, increased rates of seismic activity are reported in the vicinity of injection wells and attributed to fluid injection [*Roeloffs and Denlinger*, 2009; *Horton*, 2012; *Ellsworth*, 2013; *Keranen et al.*, 2013; *Kim*, 2013; *Frohlich et al.*, 2014; *McGarr*, 2014; *Schultz et al.*, 2014]. While the fundamental geomechanical processes linking fluid injection and seismic fault slip are well known and documented [*Raleigh et al.*, 1972; *Hsieh and Bredehoeft*, 1981; *Cappa and Rutqvist*, 2011; *Evans et al.*, 2012; *National Research Council*, 2013; *Jha and Juanes*, 2014; *Segall and Lu*, 2015], the correlation between injection activity and the occurrence of seismic events is in many cases based on their spatial and temporal association, some with a pore pressure disturbance analysis but without a site-specific geomechanical analysis [*Ake et al.*, 2005; *Frohlich et al.*, 2011; *Frohlich*, 2012; *Keranen et al.*, 2013; *Frohlich and Brunt*, 2014; *Frohlich et al.*, 2014; *Hornbach et al.*, 2015]. Because the onset of induced seismic activity depends not only on the magnitude of pore pressure disturbance in response to injection but also on in situ stress conditions and the presence and orientation of faults in the vicinity of the injection well, we propose that a complete hazard assessment for induced seismicity has to contain a site-specific geomechanical analysis. For evaluating the potential for induced seismic fault slip during the design phase of injection programs, site assessments that consider the coupled geomechanical and reservoir flow processes are desirable to optimize fluid injection strategies while minimizing potentially associated seismic hazards. Such a site assessment considers rates and volume of fluid injection that the target formation can accommodate without attaining critical reservoir pressures for reactivation of nearby faults [*Lucier et al.*, 2006; *Rinaldi and Rutqvist*, 2013; *Konstantinovskaya et al.*, 2014]. This study provides a coupled geomechanical and reservoir flow model for the 2012 Timpson M_w4.8 seismic event in east Texas to assess if the volume and rate of fluid injected into disposal wells are sufficiently high to induce seismic fault slip on nearby faults and if the observed delay between onset of fluid injection and earthquake activity is consistent with modeled rates of fluid pressure diffusion in the reservoir layer.

The 17 May 2012 M_w4.8 earthquake near Timpson, east Texas, occurred 69 months after wastewater injection commenced into two nearby disposal wells. The M_w4.8 event followed a sequence of smaller earthquakes that started in April 2008, 17 months after the start of wastewater injection [*Frohlich et al.*, 2014]. These two wells, referred to as South and North wells, are located within 3 km of the epicentral region and target
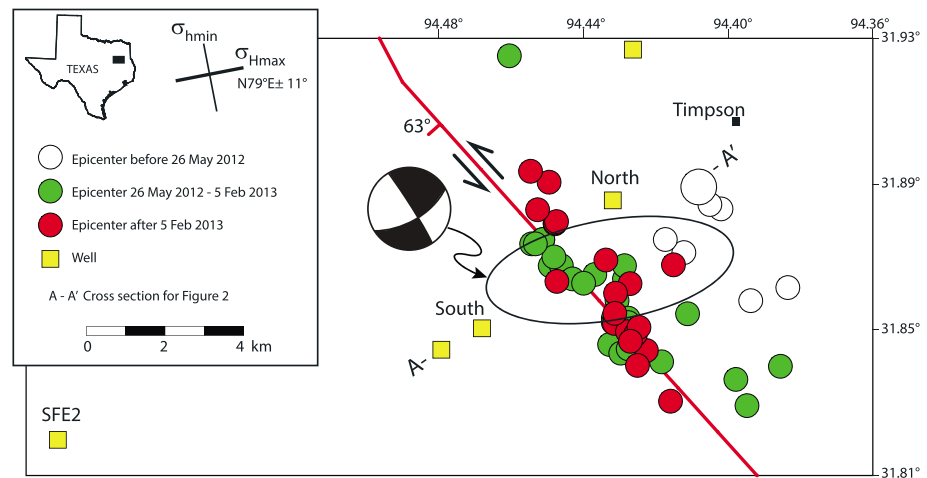
Figure 1. Map of epicenters for the earthquake sequence near Timpson, east Texas (modified after *Frohlich et al.* [2014]). The main $M_w4.8$ event (beach ball diagram) likely occurred within the elliptical region approximately defined by the Mercalli intensity MMI VII area. Red circles are the most reliable epicenter locations of aftershocks after deployment of temporary stations in February 2013. These best located aftershocks align along a mapped fault striking about N42°W. In situ stress orientations are determined using wellbore breakout and drilling-induced fracture data from SFE2 well showing the orientation of maximum horizontal stress σ_{Hmax} of N79°E ± 11°.

the Rodessa Formation of the Trinity Group, an oolitic sandstone [*Frohlich et al.*, 2014] (Figure 1). The Rodessa Formation is overlain by fine crystalline anhydrite with interbedded limestone and dolomite of the massive anhydrite and underlain by limestone of the James Lime. The South well became operational in August 2006, with an average injection rate of 42,750 m³/month at an average surface pumping pressure of 11.7 MPa, injecting at depths between 1853 and 1868 m [*Frohlich et al.*, 2014; *Texas Railroad Commission*, 2014]. At the North well starting in February 2007, wastewater is injected at depths between 1897 and 1910 m at an average surface pumping pressure of 13.6 MPa. As of December 2012, the total injected volume for the North and South wells are 1.05 and 2.9 million cubic meters, respectively. Epicenters of smaller events following the $M_w4.8$ event and located using a portable seismic array are aligned parallel to a fault that was previously mapped using seismic reflection surveys [*Jackson*, 1982; *Frohlich et al.*, 2014]. Focal depths of these events range between 1.6 and 4.6 km. The $M_w4.8$ event is the largest recorded earthquake to date within a region where historical earthquakes are rare [*Frohlich and Davis*, 2002].

To investigate the causal relationship between fluid injection and initiation of seismic fault slip, we integrate geological and geophysical data into a finite element model and conducted coupled poroelastic simulations to estimate stress changes and pore pressure perturbations associated with wastewater injection and to evaluate the potential of fault reactivation. In addition to exploring the causal links between fluid injection and earthquake activity, we seek to quantify how uncertainties in model input parameters such as reservoir permeability and fault and stress orientation influence fault stability predictions. We find that an injection-induced origin of the $M_w4.8$ event at Timpson is plausible within the admissible range of input parameters although model outcomes are sensitive to variations in input parameters that are within their observational uncertainties.

2. Methods

2.1. Model Configuration and Boundary Conditions

Using the software package Abaqus, we constructed a plane strain poroelastic finite element model to simulate the time-dependent distributions of pore pressure and effective stress in the injection layer and in the overlying and underlying units. The simulation plane is oriented NE-SW, perpendicular to the fault, and contains both injection wells (Figure 1). The model extends from the surface to a depth of 4 km and consists of 14 layers (Figure 2), with porosity, permeability, and poroelastic parameters listed in Table S1. Tops of formation were taken from logs of the South well obtained through the Texas Railroad Commission database [*Texas Railroad*
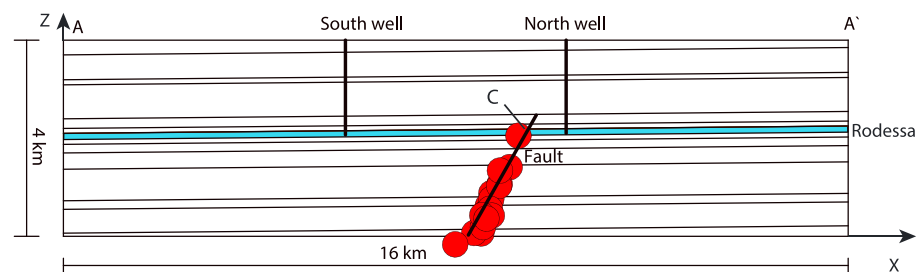
Figure 2. Finite element model geometry. Red circles are reliably located hypocenters in section A-A' which coincide with the mapped fault dipping about 63° to the SW. C: Location of Coulomb failure stress calculation (Figure 5).

Commission, 2014]. The distance between the two injection wells is 4.5 km. The regional bedding dip is about 0.6° to the SW based on *Ewing's* [1990] tectonic map. We extend the model horizontally to 16 km to minimize lateral boundary effects. The multilayered domain is intersected by the fault dipping about 63° to the southwest. We locate the fault along the aftershock cluster shown in Figure 2 which is located ~1 km NE of the fault mapped by *Jackson* [1982] (Figure 1). Based on the aftershock locations, we determined the fault orientation as strike—N42°W $\pm$ 5°, dip 63° $\pm$ 2° to the SW. In the base scenario of simulation, the fault is represented as an embedded interface with zero thickness and mechanical properties equal to those of the surrounding formations and thus transparent to fluid flow. We have insufficient information to determine the dip-slip stratigraphic offset along the fault, which we assumed to be negligible for the outcome of the simulations. The effect of fault architecture and permeability structure on fluid flow, pore pressure distribution, and fault stability will be discussed in section 3.3.

The injection is simulated by applying a constant flow rate to nodes in the perforated interval of the injection wells. We approximate the 3-D geometry of fluid injection in the 2-D finite element simulation by assuming that injection occurs from a planar source that is oriented perpendicular to the model plane, with height equivalent to the perforated interval, and extending for 3 km to each side of the model plane. This distance is equivalent to the approximate distance of the well bore to the fault. We inject wastewater into the South well at a constant velocity of 3.9 m/s, corresponding to a reported volumetric injection rate of 4.27×10^4 m³/month, and into the North well at 1.0 m/s, corresponding to 1.56×10^4 m³/month. The duration of fluid injection in our simulation is 8 years (96 months).

The 2-D plane strain numerical approach was selected for computational efficiency, following the two-step approach described by *Rutqvist et al.* [2008] by first calculating the coupled flow and poroelastic stress changes in the model plane in Abaqus. The stress and fault stability analysis was then performed in three dimensions including calculating the out-of-plane stress components assuming that the material properties are isotropic. Because of the uncertainties of stress orientations, the model plane is oriented 15°–47° relative to the maximum horizontal principal stress, with the uncertainties in stress orientation considered in the fault stability analysis.

Boundary conditions of the model domain are as follows:

Top: traction free, $p = 0$
Bottom: $v = 0$, $p = 0$
Left and right: $u = 0$, $p = 0$

where u and v are horizontal and vertical displacements, respectively, and p is excess pore pressure. In situ stress conditions were determined as part of this study using image logs of the SFE2 well (Figure 1) as described in section 2.3. Available reservoir pressure data [*Texas Railroad Commission*, 2014] indicate that the Rodessa Formation was moderately underpressured prior to injection, with a bottom hole pressure at a depth of 1844 m in the south well of 17.2 MPa.

To account for the pressure effects of production from the Rodessa Formation prior to wastewater injection and to create a pore pressure field matching these available data, we simulate continuous fluid production at a constant extraction rate (one tenth of the injection rate) at the two wells for 6 years, assuming an initial nominal hydrostatic pore pressure and no regional head gradient. The initial nominal hydrostatic pressure

of 19 MPa is based on a depth-averaged fluid density of 1050 kg/m^3 (calculated using data from *Texas Water Development Board* [1972]). Free flow of fluid is then allowed to achieve equilibrium until the bottom hole pressure of 17.2 MPa is reached at the South well and fluid injection is initiated.

Using a compression positive convention, we assume that the onset of seismic fault slip is adequately described by the friction criterion

$$CFS = \tau - \mu(\sigma_n - p) \tag{1}$$

where CFS is the Coulomb failure stress, μ is coefficient of friction, p is pore fluid pressure, and τ and σ_n are shear and total normal stresses acting on the fault, respectively, which in turn are affected by the pore fluid pressure diffusion due to the poroelastic effect. We assume negligible cohesion for seismic slip on a preexisting fault surface. Assuming that the slip criterion for the fault is met first where the fault transects the injection layer, we calculate the Coulomb failure stress at point C on the fault, at the top of the injection layer (Figure 2).

2.2. Numerical Simulation of Coupled Pore Pressure and Stress Change

The poroelastic constitutive relationship is implemented by Abaqus as follows. For the volumetric response, the change in void ratio e is related to the mean Terzaghi effective stress through [*Abaqus*, 2014; *Luo et al.*, 2015]

$$de = -\kappa d\ln\sigma'_m \tag{2}$$

where $\sigma'_m = 1/3\ \sigma'_{kk}$ is the mean Terzaghi effective stress. The parameter κ is the logarithmic bulk modulus given by [*Luo et al.*, 2015]

$$\kappa = \frac{1 + e_0}{K_s(1 - \alpha)}\sigma'_m \tag{3}$$

where e_0 is the initial void ratio, K_s is the bulk modulus of the solid grain, and α is the Biot coefficient which characterizes the efficiency of pore pressure in counteracting confining pressure to generate volumetric strain [*Wang*, 2000]. The relationship between void ratio e and porosity ϕ is $e = \phi/(1 - \phi)$. For fully saturated rocks, the Terzaghi effective stress σ'_{ij} is related to the total stress σ_{ij} and pore pressure p through

$$\sigma'_{ij} = \sigma_{ij} - p\delta_{ij} \tag{4}$$

where δ_{ij} is the delta function. The deviatoric response is defined by

$$de_{ij} = \frac{1}{2G}ds_{ij} \tag{5}$$

where s_{ij} and e_{ij} denote the deviatoric stress and strain, respectively, and G is the shear modulus. Fluid flow follows Darcy's law. In the Abaqus simulation of fully coupled poroelasticity problems, the finite element mesh is attached to the solid skeleton while allowing fluid flow through the mesh by using continuum pore pressure elements whose nodes have displacement and pore pressure degree of freedom. We refer to *Abaqus* [2014] for details on the solution strategy and to *Altmann et al.* [2010] for a validation against analytical solutions for a point injection into a 3-D isotropic space by *Rudnicki* [1986] (see also *Abaqus* [2014], for other benchmark solutions).

The simulation was carried out in Abaqus using eight-node plane strain elements equipped with biquadratic displacement and bilinear pore pressure basis functions. At the interface between two adjacent layers, displacement, total stress, and pore fluid pressure are assumed to be continuous.

2.3. In Situ Stress Determination

We constrained the in situ stress using borehole televiewer images for the SFE2 well, located 14 km from the epicenter. The image logs, collected in 1987, recorded both wellbore breakouts and drilling-induced fractures indicating that the well experienced both shear and opening-mode failure as it was drilled [*Laubach et al.*, 1988; *Plumb*, 1989] (Figure 3a). The drilling-induced fractures are parallel to the axis of the vertical well which indicates that vertical stress σ_v is a principal stress and the minimum compressive horizontal stress σ_{hmin} is the least principal stress [*Zoback et al.*, 1985]. For clearly discernible breakouts, we measured the combined width of the dark bands in the borehole televiewer image and determined the breakout width as breakout width = $180 \times$ (sum of dark bands width)/(width of unwrapped image). The azimuth of σ_{hmin} was measured at the midpoint of the dark bands. We measured 136 breakout azimuths and 408 breakout widths at 0.1 foot
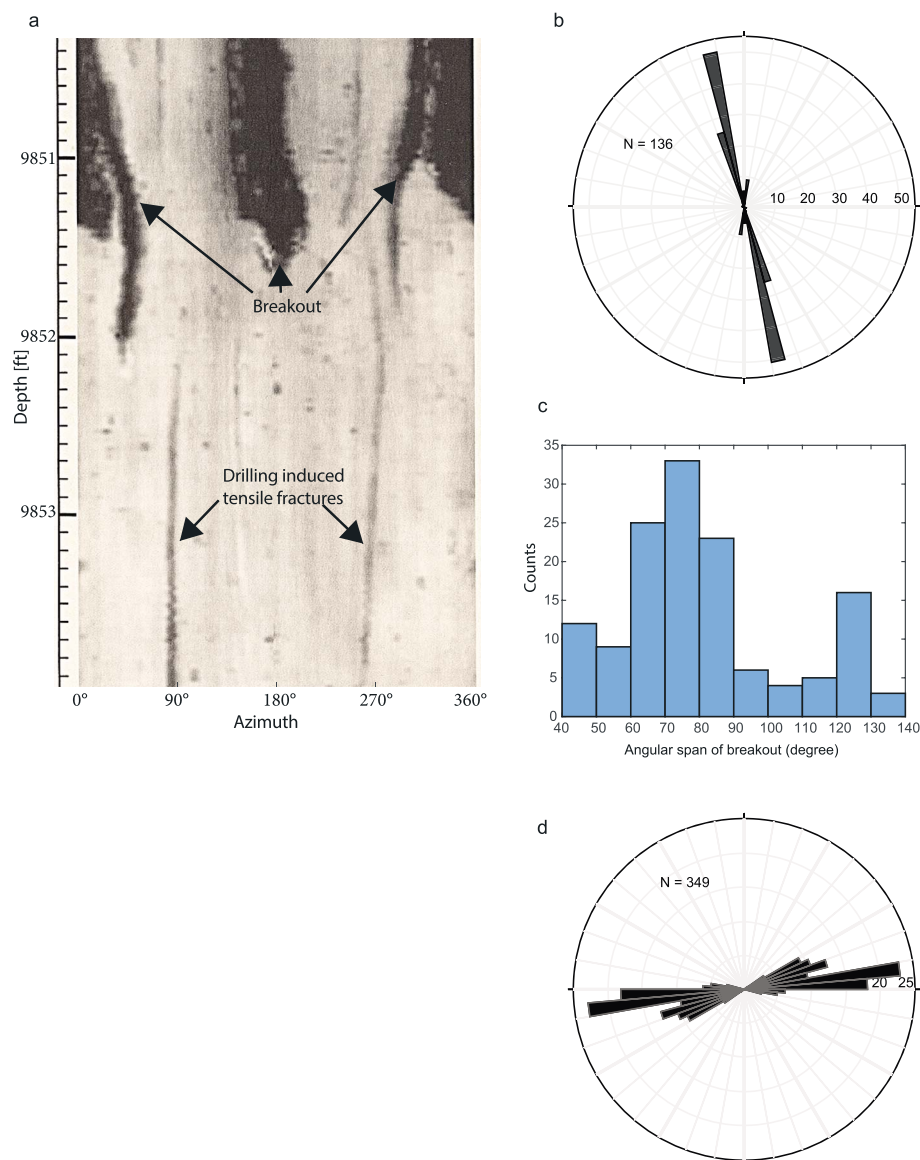
Figure 3. (a) A representative borehole televiewer image for the SFE 2 well with breakouts (dark bands) and drilling-induced tensile fractures (black lines). (b) Wellbore breakout azimuth distribution, (c) breakout angular span, and (d) drilling-induced fractures distribution in the SFE2 well. See Figure 1 for well location.

(3.05 cm) depth increments in five distinct breakout zones with a cumulative length of 4.6 m over a depth range of 514 m (measured depths of 8254–9938 ft, 2515–3029 m), providing a minimum compressive horizontal principal stress orientation of N166 ± 3°E (Figure 3b). Hence, the mean σ_{Hmax} orientation is N76° E. The angular breakout is 71° ± 13° (Figure 3c). Four distinct drilling-induced fractures were detected covering a cumulative length of 17 m in the measured depth interval of 9678–9931 ft (2950–3027 m), with 349 measurements yielding a mean orientation of σ_{Hmax} of N79°E ± 11° (Figure 3d). Wellbore breakout data were assigned C quality according to the quality ranking system for stress indicators by *Zoback* [2010] and D quality based on the ranking system by *Heidbach et al.* [2010]; drilling-induced fracture data are assigned D quality in both ranking systems. Combining the azimuth information of wellbore breakouts and drilling-induced fractures in the SFE 2 well, we determined an average σ_{Hmax} azimuth of N79 ± 11°E. The inferred direction of σ_{Hmax} derived from our measurement is consistent with the stress orientation independently determined by *Laubach and Monson* [1988] using coring-induced fractures observed in oriented core from the SFE2 well and with the in situ σ_{Hmax} direction of N68°E reported for the closest well by *Heidbach et al.* [2008].

Table 1. Magnitude of Maximum Horizontal Stress Obtained From SFE2 Wellbore Breakout Data[a]

Depth (m) of Breakout	P (MPa)	σ_V (MPa)	σ_{hmin} (MPa)	UCS (MPa) Values Reported Closest to Breakout Depth	σ_{Hmax} (MPa)
2516	25.8	*60.4*	35.2	*64*	*57.2–72.7*
				128	88.3–125.7
				197	121.8–182.7
3013	31.0	*72.3*	42.2	*51*	*56.1–65.9*
				74	*67.3–84.9*
				321	187.2–289.2
3029	31.2	*72.7*	42.4	*51*	*56.3–66*
				74	*67.4–85*
				321	187.3–289.3

[a]Numbers in italic are consistent with σ_{Hmax} approximately equal to σ_v when the lower range of measured UCS values is used.

An average gradient of the vertical stress σ_v of 24 MPa/km was calculated by *Thiercelin and Plumb* [1994] through integration of the bulk density log of the SFE2 well. Using the microfrac technique, the minimum horizontal stress σ_{hmin} was determined by *Peterson* [1989] to be 41.9 MPa at a depth of 3014 m. Utilizing breakout width determined above and unconfined compressive strength (UCS, also referred to as cohesive strength C_0) data reported by *Plumb et al.* [1992], and assuming a hydrostatic pore pressure gradient, the magnitude of the maximum compressive horizontal principal stress σ_{Hmax} is obtained through

$$\sigma_{Hmax} = \frac{C_0 + 2P - \Delta P_w - \sigma_h(1 - 2\cos\omega_{bo})}{1 + 2\cos\omega_{bo}} \tag{6}$$

where ΔP_w is the difference between the wellbore pressure and the pore pressure, which is assumed to be negligible, and ω_{bo} is the breakout width [*Zoback et al.*, 1985]. *Plumb et al.* [1992] measured UCS for eight selected rock samples collected from the SFE2 well between the depths of 2513 and 3030 m. Their results range from 51 to 321 MPa. The presence of wellbore breakouts requires that the maximum hoop stress along the wellbore exceeds the UCS of the rock. We calculated σ_{Hmax} for all the UCS values (Table 1), but because breakouts are expected to occur preferentially in weaker lithologies, values calculated using the lowest UCS values give the best estimate of σ_{Hmax}. The results, summarized in Table 1, suggest that the magnitude of σ_{Hmax} is approximately equal to σ_v when the lower values of measured UCS values are used. In addition, an estimate of σ_{Hmax} using $\sigma_{Hmax} = (3\sigma_{hmin} - 2P)$ [*Zoback*, 2010] and assuming a negligible tensile strength gives a value of σ_{Hmax} of approximately 64 MPa at a depth of 3003 m, close to the vertical stress of 72 MPa. σ_{Hmax} constrained from strike-slip earthquake focal mechanism indicates that $\sigma_{Hmax} \geq \sigma_v$. Combining these lines of evidence, it is reasonable to take $\sigma_{Hmax} = \sigma_v$, i.e., a transitional stress state between a strike slip and normal faulting stress regime, as the starting condition of our simulations, prior to the start of production and injection.

Once the in situ stress tensor σ in the principal coordinate system is known, the stress in the modeling system (xyz) can be obtained via the tensor transformation [*Peška and Zoback*, 1995]

$$\sigma^m = A^T \sigma A \tag{7}$$

where $A = \begin{bmatrix} \sin(az + st) & -\cos(az + st) & 0 \\ \cos(az + st) & \sin(az + st) & 0 \\ 0 & 0 & 1 \end{bmatrix}$ is the transformation matrix, with az and st denoting the

azimuth of σ_{Hmax} and the fault strike, respectively. $\sigma = \begin{bmatrix} \sigma_{Hmax} & 0 & 0 \\ 0 & \sigma_{hmin} & 0 \\ 0 & 0 & \sigma_V \end{bmatrix}$ is the stress in the principal coor-

dinate system. The normal stress σ_n and shear stress τ acting on the fault are given by [*Peška and Zoback*, 1995]

$$\sigma_n = n_1^2 \sigma_{Hmax} + n_2^2 \sigma_{hmin} + n_3^2 \sigma_V \tag{8}$$

$$\tau = \sqrt{n_1^2 \sigma_{Hmax}^2 + n_2^2 \sigma_{hmin}^2 + n_3^2 \sigma_V^2 - \left(n_1^2 \sigma_{Hmax} + n_2^2 \sigma_{hmin} + n_3^2 \sigma_V\right)^2} \tag{9}$$

where $n_1 = \cos(dip + 90°)\cos(az + st - 90°)$, $n_2 = \cos(dip + 90°)\cos(180° - az - st)$, and $n_3 = \cos(dip)$ are the

components of the unit normal to the fault plane with dip denoting the fault dip angle.

During fluid injection, total stress and pore pressure are coupled by the poroelastic effect with an increase in pore pressure causing a poroelastic increase in total compressive horizontal stresses, which in turn influences the normal stress acting on the fault. Because of the traction-free boundary condition at the Earth's surface, and the large width to height ratio of the pressure disturbance in the reservoir at advanced stages of fluid injection, the vertical total stress will remain constant. During the simulation, we stored the pore pressure and Terzaghi effective horizontal stress (equation (4)) at each time step for all the nodes. We find the node along the preexisting fault which undergoes the maximum pore pressure changes, extract the pressure and stress history from Abaqus, and then substitute the total stress into equations (8) and (9) to calculate the normal stress and shear stress resolved on the fault. The Coulomb stress as a function of time at that point is obtained from equation (1). When the Coulomb stress at that point on the fault changes from negative to positive, shear failure is assumed to occur. For the Coulomb failure stress calculation, we assume a coefficient of friction of 0.6, representing the low end of values reported by *Byerlee* [1978] of 0.6–0.85. The low friction coefficient favors fault reactivation, thus providing a conservative estimate of fault stability. These results will be compared to those using higher friction coefficients.

3. Results

3.1. Effect of Permeability of Injection Layer on Fault Stability

We first examine the effect of permeability of the injection layer on pore pressure diffusion, stress distribution in the reservoir, and Coulomb shear stress on the fault. Figures 4a–4c show the excess pore pressure profile after 69 months of fluid injection, corresponding to the duration between onset of injection and the M_w4.8 event, for a permeability of the injection layer of 200 mdarcy (base case), 100 mdarcy, and 400 mdarcy, respectively. This range in permeability is within the range of 10–650 mdarcy reported for the Rodessa Formation by *Mancini et al.* [2012] [Table S1]. Under otherwise identical conditions, pore pressure changes are higher in an injection layer of lower permeability compared to a layer of higher permeability. Higher permeability corresponds to a higher diffusivity, which allows faster diffusion of fluid. Because we assume a constant injection rate for the two injection wells, it will take longer for pore pressure to build up adjacent to the fault and thus trigger fault slip in an injection layer of higher permeability. Since the permeabilities of overlying and underlying strata are 3 to 4 orders of magnitude lower than that of the injection layer, the migration of wastewater is primarily occurring in the Rodessa layer, with additional fluid migration into underlying strata. We note that pore pressure decreases with increasing distance away from the injection well until it meets the diffusive fluid pressure front propagating from the second injection well. This decrease in pore pressure with increasing distance becomes more pronounced as permeability of the injection layer decreases. Consequently, two expanding pore pressure anomalies or bulbs form around the wells, which are commonly observed for high-volume fluid injection [*Nicholson and Wesson*, 1990]. The pore pressure anomalies are more pronounced for the case of lower permeability of the injection layer. For the base scenario with an injection layer permeability of 200 mdarcy, the simulated pore fluid pressure increase at the North well after 69 months of injection is 13.7 MPa and the maximum pore pressure perturbation along the fault (denoted by point C in Figures 2 and 4) is 12.9 MPa at a distance of about 800 m from the North well.

For a given permeability of the injection layer, the simulated pore pressure increases monotonically with time, which counteracts the normal stress and decreases the Terzaghi effective normal stress (Figures 5a–5c). As a result, the Coulomb failure stress also increases with time, which means that the potential for fault reactivation is enhanced. After 6 months of injection at the South well, the North well becomes operational (dashed vertical lines in Figure 5), which causes a second stage of rapid increase in pore pressure. After about 500 days (16 months), the rate in excess pore pressure increase slows down considerably as a result of increasing fluid migration into underlying strata with increasing reservoir pressure. Comparing the results for $k = 200$ mdarcy, 400 mdarcy, and 100 mdarcy (Figures 5a–5c), we observe that, at any given time, a lower permeability of the injection layer increases the pore fluid pressure, decreases the effective normal stress, and thus increases the Coulomb failure stress. Thus, a lower permeability of the injection layer results in a higher potential of fault slip and potentially an earlier onset of seismic activity. For the base scenario ($k = 200$ mdarcy, Figure 5a) the Coulomb failure stress remains negative which means that the fault remains stable for the entire duration of 96 months of simulated injection. For a permeability of the injection layer of 100 mdarcy, the simulation predicts faults slip after 745 days or 25 months, which is 7 months later than the observed onset of seismicity at 17 months after injection (star in Figure 5b). However, unlike the base case where the least effective Terzaghi
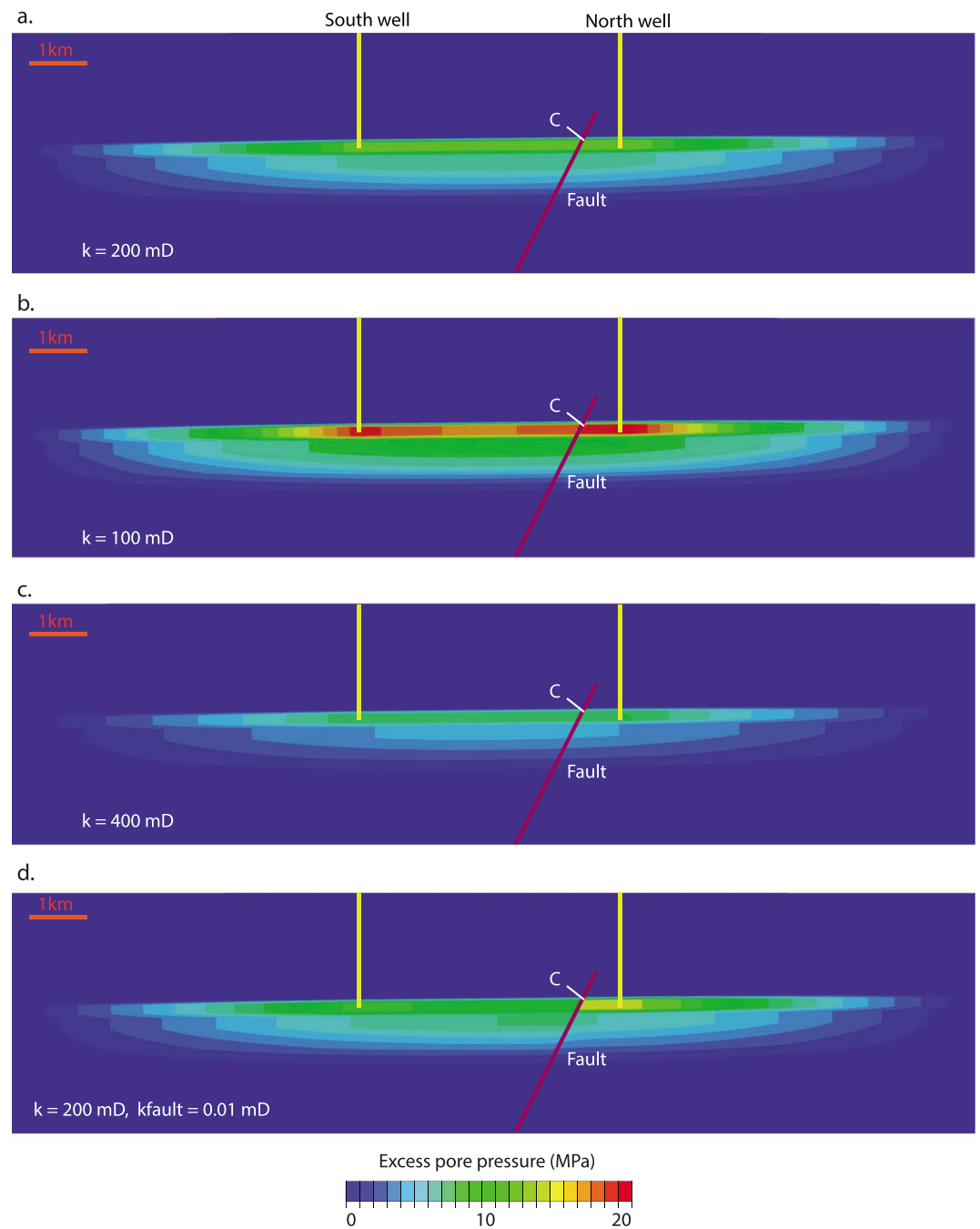
Figure 4. Pore pressure profiles after 69 months of injection for permeabilites of the injection layer of (a) 200 mdarcy, (b) 100 mdarcy, and (c) 400 mdarcy. Fault properties are those of the formation. (d) Pore pressure profile after 69 months of fluid injection for a sealing fault (k_{fault} = 0.01 mdarcy; $k_{formation}$ = 200 mdarcy). C: location of Coulomb failure stress calculation (Figure 5).

principal stress $\sigma'_3 = \sigma'_{hmin}$ remains compressive, this stress becomes tensile in the 100 mdarcy layer after 716 days or 24 months of injection (dotted vertical line in Figure 5b), allowing hydraulic fractures to form. These hydraulic fractures would be oriented at about 59° relative to the fault, thus possibly conducting the injection fluid toward the fault. Because induced hydraulic fractures will effectively increase the reservoir permeability, we will use a reservoir permeability of 200 mdarcy as the permeability most prone for fault instability without leading to hydraulic fracture for all subsequent simulations addressing effects of varying fault and stress orientation and fault permeability on fault stability.
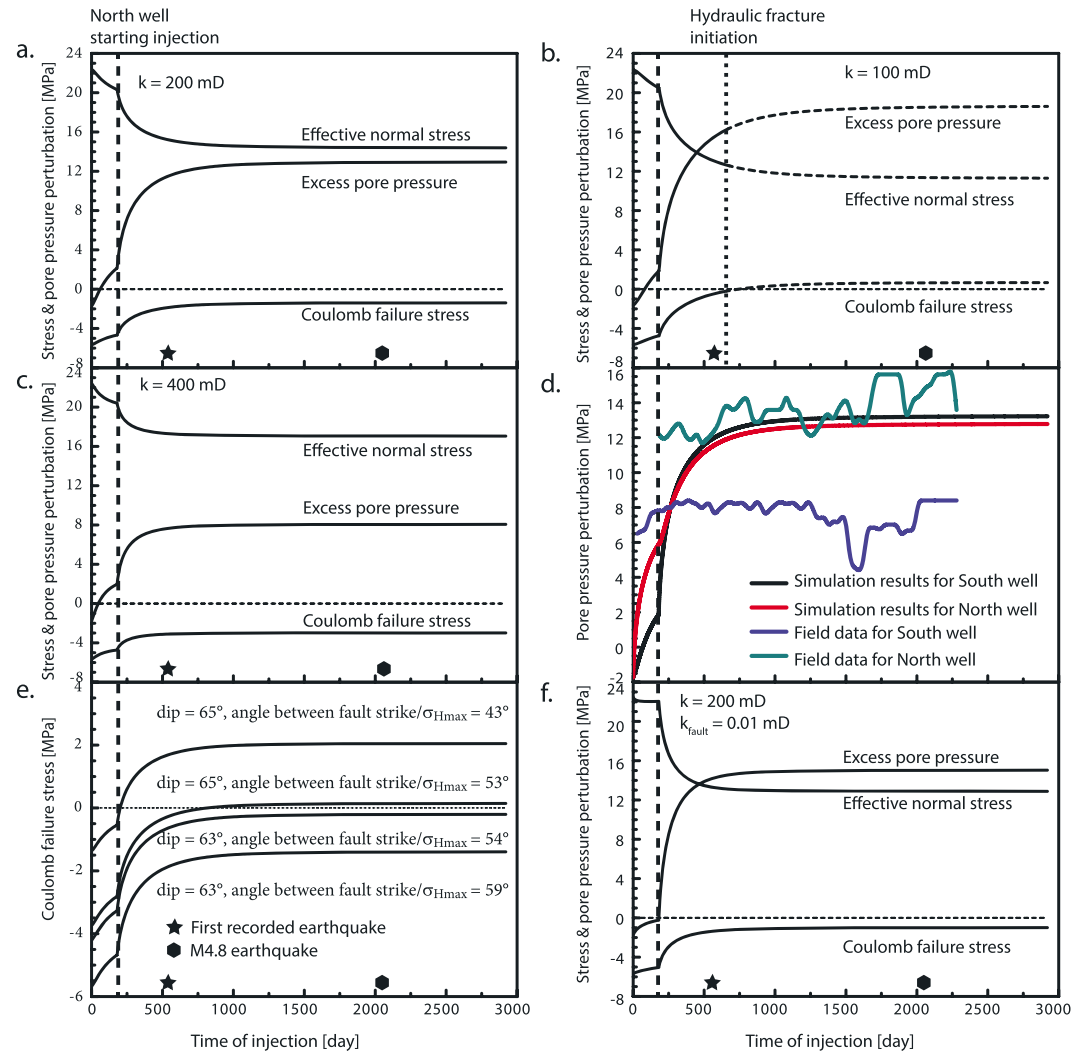
Figure 5. Evolution of Coulomb failure stress, excess pore pressure, and Terzaghi effective normal stress on fault at point C, as a function of reservoir permeability k. Coulomb failure stress calculated for fault orientation N42°W/63°SW, azimuth of σ_{Hmax} N79°E, and coefficient of friction of 0.6. (a) $k = 200$ mdarcy, (b) $k = 100$ mdarcy, and (c) $k = 400$ mdarcy. (d) Comparison of simulated bottom hole pressure and bottom hole pressure calculated from measured surface injection data taking friction loss into account; see text for discussion. (e) Evolution of Coulomb failure stress over time at point C along the fault for different combinations of fault orientation and in situ stress orientation. (f) Effect of fault permeability on the pore pressure and stress evolution as a function of time at point C, located on the footwall of the low-permeability ($k = 0.01$ mdarcy) fault. Formation permeability $k = 200$ mdarcy.

To validate our numerical results, we compare simulated excess pore pressure at the bottom of the two injection wells to bottom hole pressures calculated from recorded surface injection pressures corrected for the frictional pressure loss in the wellbore (Figure 5d). The bottom hole pressure p_{bottom} is related to surface pressure through $p_{bottom} = p_{surface} + p_{hydro} - p_{friction}$, where $p_{surface}$ is the recorded surface injection pressure, p_{hydro} is the hydrostatic pressure created by fluid weight, and $p_{friction}$ is the pressure loss due to friction. $p_{friction}$ is given by [*Economides and Martin*, 2007]

$$p_{friction} = 2f\frac{\rho_{fluid}Lv^2}{d} \tag{10}$$

The parameter ρ_{fluid} is the fluid density (1050 kg/m^3), L is the length of the pipe in meters, v is the velocity in m/s, d is the pipe inside diameter in meters, and f is the friction factor. The friction factor can be obtained from the Reynold's number Re through $f = 0.0303/Re^{0.1612}$. The friction loss was calculated as 3.2 MPa and 0.2 MPa
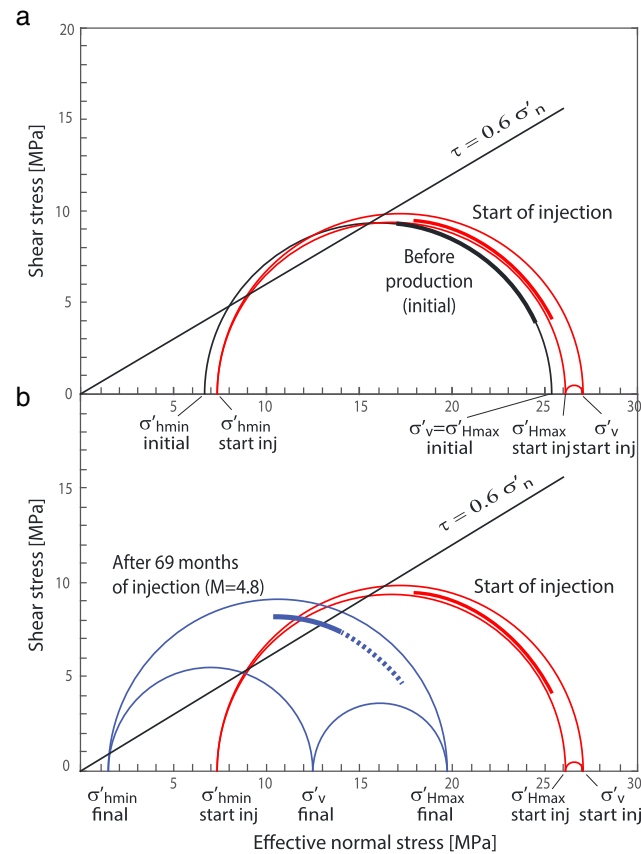
Figure 6. Change in stress state and tractions at point C along the fault (a) before (initial) and after (start inj) fluid production and (b) at the start of (start inj) and after 69 months (time of M_W4.8 event) of fluid injection. Criterion for frictional slip on a cohesionless fault assumes a Byerlee coefficient of 0.6. Heavy black circle segment in Figure 6a represents initial tractions at point C along the fault for an admissible range of fault and in situ stress orientations. Heavy red circle segment in Figures 6a and 6b indicates tractions at point C along the fault prior to injection. Heavy blue circle segment in Figure 6b indicates stress states at point C along the fault after 69 months of fluid injection. Dashed segment of heavy blue circle segment indicates stress conditions leading to hydraulic fracture prior to fault slip (least compressive horizontal Terzaghi effective stress $\sigma'_{hmin} = 0$).

for the South and North wells, respectively, using well diameters of 0.07 and 0.09 m [*Texas Railroad Commission*, 2014]. Because we use a constant injection rate equivalent to a 6 year average, the numerical simulation yields a smooth pore pressure response, compared with the monthly varying field data. Comparing these bottom hole pressures to the excess pore pressure obtained in the Abaqus simulation using a specified constant flow rate, we get a reasonably close fit for the North well but overestimate the pressure in the South well (Figure 5d). The close fit for the North well suggests that our injection geometry reasonably approximates the 3-D field geometry. The mismatch in the South well may reflect regional variations in injection layer permeability not accounted for in the simulation. Because the fault is located more closely to the North well, the mismatch with the South well injection pressure should have a lesser effect on predicting fault slip.

3.2. Effect of Uncertainties in Fault and In Situ Stress Orientation on Fault Stability Estimation

The precision of aftershock hypocenter locations reported by *Frohlich et al.* [2014] of about 0.5 km (Figures 1 and 2, C. Frohlich, oral communication, 2015) leads to an admissible range of fault strike of N42°W ±5° and dip 63°±2° to the SW. The orientation of σ_{Hmax} as determined above is N79°E ± 11°. To assess the sensitivity of fault reactivation on variation in fault orientation and in situ stress orientation, we simulated the evolution of Coulomb failure stress over time using four different admissible combinations of fault strike, fault dip, and azimuth of σ_{Hmax} within their range of uncertainties, assuming an injection layer permeability of 200 mdarcy. (Figure 5e). Increasing fault strike azimuth, dip angle, or the azimuth of σ_{Hmax} will orient the fault more favorably for slip relative to the principal stress orientations, expressed as an increase of Coulomb failure stress. This can be explained by observing the normal and shear stress resolved across the fault in equations (8) and (9). For the most favorably oriented fault orientation, seismic slip is predicted to occur after 215 days or 7 months of injection (Figure 5e). We note that the Coulomb failure stress is highly sensitive to small variations in fault or stress orientation.

The effect of changing pore pressure and stress state at point C along the fault is displayed in Figure 6 using a 3-D Mohr diagram for Terzaghi effective stress. The initial effective stress state prior to production from the Rodessa layer, with $\sigma'_{Hmax} = \sigma'_V$, is represented by a single Mohr circle, with the range in fault orientation relative to the principal stress orientations indicated by the bold segment of the stress circle. A decrease in pore pressure due to production causes an increase in differential stress in addition to the increase in Terzaghi effective stress. The Mohr circle is driven to the right, away from the friction line (Figure 6a). Because the fault

Table 2. Variations of Fluid Pressure Increase Along the Fault and Time Lag Between Start of Fluid Injection and Fault Reactivation for Different Combinations of Injection Layer Permeability, Fault Orientation, and In Situ Stress Orientation[a]

Permeability of Injection Layer (mdarcy)	Fault Strike	Fault Dip, Dip Direction	Azimuth of Maximum Horizontal Stress	Maximum Pore Pressure Perturbation Along the Fault (MPa)	Time Lag Between Start of Fluid Injection and Initiation of Fault Slip (Months)
200	N42°W	63°SW	79°NE	12.9	no slip
400	N42°W	63°SW	79°NE	8.1	no slip
100	N42°W	63°SW	79°NE	18.6	hydraulic fracture
200	N47°W	63°SW	79°NE	12.9	no slip
200	N37°W	63°SW	79°NE	12.9	no slip
200	N42°W	65°SW	79°NE	12.9	no slip
200	N47°W	65°SW	80°NE	12.9	27
200	N42°W	63°SW	90°NE	12.9	11
200	N47°W	65°SW	79°NE	12.9	no slip
200	N47°W	65°SW	90°NE	12.9	7

[a]"No slip" indicates no slip occurring within 8 years of simulated injection. "Hydraulic fracture" indicates that hydraulic fractures would form before the slip criterion is met on the fault.

is not favorably oriented relative to the in situ stress state, the fault is stable prior to injection. More favorably oriented faults would be unstable using a friction criterion of 0.6. We interpret these results to indicate that the stress state prior to injection is controlled by critically stressed faults that are located outside the area affected by fluid injection. After 69 months of injection, pore fluid pressure increases by 12.9 MPa, reducing the effective stress and shifting the stress state closer to the friction line (Figure 6b). Because we assume isotropic poroelastic properties, total σ_{hmin} increases at the same rate as σ_{Hmax} while total σ_v remains constant because of the traction-free Earth's surface. Terzaghi effective stress σ'_v after injection is thus lower than σ'_{Hmax}. The tractions on the fault at point C, shown for their admissible range of angles between the fault and the principal stresses (bold blue circle segment in Figure 6b), fall to both sides of the friction line, indicating that fault slip would occur earlier than 69 months for more favorable orientations, while for less favorable orientations the fault would remain stable after 69 months of fluid injection although they may become unstable with continued injection and pore pressure increase. The dashed bold blue circle segment in Figure 6b corresponds to fault orientations relative to the stress state at which hydraulic fracture would occur prior to fault slip if the pore pressure were to increase further, assuming zero tensile strength of the reservoir (least compressive horizontal Terzaghi effective stress $\sigma'_{hmin} = 0$). The fault and in situ stress orientations leading to slip on the fault are indicated by the solid bold blue circle segment. This segment corresponds to an angle between fault strike and σ_{Hmax} of 59 to 75°, for a fault dip of 65°.

Calculated excess pore fluid pressure at the fault and time lag between the onset of fluid injection and the initiation of fault slip are summarized in Table 2 for different combinations of injection layer permeability, fault orientation, and in situ stress orientation. The time delay between start of injection and onset of seismic activity obtained in these simulations ranges from 7 months of fluid injection to no seismic event observed within the simulated injection duration of 96 months, highlighting the sensitivity of fault slip potential predictions on model input parameters.

Fault stability and time lag between onset of injection and fault slip were obtained using a conservative coefficient of friction of 0.6. Increasing the coefficient of friction to 0.7, an intermediate value [*Byerlee*, 1978], extends the onset of seismicity from 7 months of fluid injection to 11 months for the most favorable fault orientation; no slip occurs within 8 years of simulated injection for a friction coefficient of 0.85. We note that a friction coefficient of 0.6 has been inferred to characterize friction of hydraulically conductive active faults [*Barton et al.*, 1995; *Ito and Zoback*, 2000]. A friction coefficient of 0.6 is assumed for the remainder of this paper.

3.3. Effect of Fault Zone Permeability on Fault Stability

The simulations presented so far considered the fault to be transparent to flow, with fault material properties equal to those of the host rock, equivalent to a zero-thickness interface. For an alternative model of fault fluid flow behavior, we now consider a fault zone of finite width composed of a fault core bounded by a damage

zone. Whether a fault acts as conduit or barrier for fluid flow across or along the fault depends on stratigraphic juxtaposition, fault zone architecture, and permeability structure of the fault core and damage zone [*Caine et al.*, 1996; *Bense et al.*, 2013], details that are not known for the fault of interest.

To assess the effect of fault zone properties on our model results, we assume the fault to be 15 m thick and composed of a low-permeability core ($k_{fault} = 0.01$ mdarcy; $k_{formation} = 200$ mdarcy) (Figure 4d). Compared to the transparent fault where the pore pressure fields starting from the two injection wells overlap to generate a combined smooth pore pressure field, we observe a sharp pore pressure discontinuity across the sealing fault resulting in an overall higher pore fluid pressure in the footwall of the fault facing the North well and lower pore fluid pressure in the hanging wall. Because the criterion for frictional slip needs to be met on only one side of the fault, with slip occurring along the interface of the fault core and the footwall or hanging wall, a sealing fault is more favorable to fault reactivation. For a formation permeability of 200 mdarcy, even though the excess pore pressure in the footwall of the sealing fault is higher than that for the transparent fault (Figure 5a), the Coulomb failure stress is still too low for fault slip to occur (Figure 5f).

4. Discussion

4.1. Coupling Between Fluid Flow and Geomechanical Deformation

In some sequences of inferred induced seismicity, fault reactivation followed fluid injection with a delay of several days or weeks [*Zoback and Harjes*, 1997]. In others, the time delay reached years or decades [*Nicholson and Wesson*, 1992; *Keranen et al.*, 2014]. Our results demonstrate that the time required for the pore pressure at the fault to reach the threshold value depends on the reservoir permeability and fault and stress orientation, in addition to injection rate and pressure, fault permeability, and distance between the injection wells and the fault, which helps to explain the wide range in observed time delays between the start of injection and the onset of seismicity. Previous numerical simulations addressing fluid induced seismicity solved the standard fluid diffusion equation and then assumed a critical pore pressure value, regardless of fault orientation and in situ stress state, that must be reached to induce seismic fault slip [*Parotidis and Shapiro*, 2004; *Shapiro et al.*, 2013; *Keranen et al.*, 2014; *Hornbach et al.*, 2015]. This approach differs from our fully coupled poroelastic approach by neglecting the coupling between fluid flow and poroelastic stress leading to a lower diffusivity and thus slower fluid diffusion, and hence a higher pore pressure distribution through the domain when compared to the fully coupled poroelastic approach. The fully coupled modeling approach as followed in this study is expected to provide a closer prediction of the time delay between injection and fault instability.

Thermal effects of injecting cold wastewater on fault seismic response were not explicitly included in the simulations because Abaqus does not provide functionality to model thermoporoelastic effects in 2-D. The injection of wastewater that is colder than the injection reservoir will result in thermoporoelastic stress and pore pressure changes in the vicinity of the bore hole. For geothermal gradients in east Texas of 11–15°C/km [*Finley et al.*, 1984], the injected fluid is about 22–29°C colder than the formation brine. The temperature reduction causes a decrease in the total stress near the injection wellbore due to contraction [*Wang and Dusseault*, 2003; *Abousleiman and Ekbote*, 2005]. The thermally induced decrease in total stress therefore counterbalances the increase in total stress from the pore pressure increase due to the poroelastic effect. In addition, a temperature drop results in a reduction of the pore pressure. Since the injected cold water has to cool the rock matrix along the flow pathway, the temperature front propagates significantly slower than the pore pressure front in a layer of permeability comparable to the Rodessa Formation [*Wang and Dusseault*, 2003]. Thermal porous modeling of cold water injection into geothermal reservoirs by *De Simone et al.* [2013] showed that thermally induced fluid pore pressure decreases with the logarithm of distance from the injection well. Far from the injection wells, the thermally induced stress and pore pressure wane quickly [*Vilarrasa et al.*, 2014]. Thermal effects on fault stability at point C in our models are thus expected to be insignificant. It is noted, however, that cooling near the injection well increases the potential of initiating tensile fractures within the formation in the vicinity of the wellbore that will locally increase reservoir permeability.

4.2. Implications for Fluid Injection Practices

Our in situ stress results suggest that the reservoir was critically stressed for favorably oriented faults prior to injection, with the in situ stress field controlled by slip along critically stressed faults located outside the influence area of fluid injection. If critically stressed faults, i.e., faults at the frictional limit in the in situ stress field,

existed in the vicinity of the injection wells, seismic slip should have occurred at the start of injection. The delayed onset of seismicity after significant fluid injection indicates absence of such favorably oriented faults within the influence area of fluid injection. The less favorable orientation of the slipped fault relative to the in situ stress state allowed significant fluid injection prior to the onset of seismic activity.

Our simulations suggest that seismic fault instability induced by fluid injection is plausible for the Timpson earthquake sequence for a range of input parameters that is within the uncertainties of our model parameters. However, equally likely model parameters predict no seismic activity in response to injection into the North and South wells. While not satisfactory in answering the question if the Timpson earthquake sequence was the consequence of water injection or the result of unrelated natural or human causes, these results demonstrate that a geomechanics-based assessment of fault stability in response to fluid injection, and any derived prediction of allowable injection volume prior to onset of induced seismicity, require well-constrained model input parameters including fault and in situ stress orientation, initial stress magnitude and pore fluid pressure, and injection reservoir permeability. Uncertainties in reservoir permeability, modeled here with a narrow range of 100–400 mdarcy, result in a calculated excess pore pressure along the fault between 8 and 18 MPa (Figures 5a–5c). Uncertainties in fault and stress orientation result in uncertainties of excess pore pressure required for fault slip of 6 MPa (corresponding to the range in shear and effective normal stress of the solid bold circle segment in Figure 6b), for a friction coefficient of 0.6, assuming that formation of hydraulic fractures in the injection layer prior to meeting the sliding criterion would inhibit seismic fault slip. These uncertainties in input parameters not only lead to large uncertainties in predicting the time delay between onset of injection and onset of induced seismicity but also to uncertainties in predicting the volume and rate of injection that could potentially lead to induced seismicity. Geomechanical models conducted prior to injection to assess potential of induced seismicity therefore require detailed site-specific geomechanical, reservoir, and structural evaluation. Of largest concern are uncertainties in reservoir permeability and the presence and orientation of faults that are below the detection limit for reflection seismic surveys but large enough to produce felt and potentially damaging seismic events. While faults large enough to result in earthquakes of magnitudes larger than ~5 are generally resolvable in reflection seismic surveys [*Wells and Coppersmith*, 1994; *Kim and Sanderson*, 2005], smaller subseismic faults may still limit reservoir injection capacity, presenting challenges in planning fluid injection programs and assessing induced earthquake potential prior to the onset of seismic activity.

5. Conclusions

To address the geomechanical link between fluid injection and initiation of seismic fault slip in Timpson, Texas, we numerically simulated the coupled processes of fluid diffusion and stress and pore pressure changes associated with fluid injection and their effects on fault reactivation. Published and newly calculated in situ stress data based on borehole breakouts and induced fractures in the nearby SFE2 well in combination with the focal mechanism of the M_w4.8 event indicate a normal/strike-slip faulting stress regime. While the initial stress state appears controlled by critically stressed favorably oriented faults, the seismically active fault near Timpson is less favorably oriented for slip suggesting the absence of favorably oriented faults in the area affected by fluid injection and allowing for the observed time delay between injection and earthquake slip. The model simulations suggest that seismicity induced by water injection in the North and South wells is plausible within a range of likely model input parameters, whereas other equally likely input parameters predict no induced seismic activity for the reported injection history. Pore pressure perturbation and the Coulomb failure stress, quantifying the potential of the fault for shear reactivation, are sensitive to the permeability of the injection layer, fault orientation relative to the in situ stress orientation, and in situ stress magnitudes. Seismic fault reactivation is favored by low reservoir permeability and a favorable orientation of the fault relative to the in situ stress state. For the base case using most likely model parameters, fault slip is not observed within 96 months of injection. A 0.5 reduction in reservoir permeability results in hydraulic fracturing within 24 months of injection rather than shear failure on the fault; the most favorable admissible fault orientation leads to fault slip within 7 months of injection, compared to the observed onset of seismicity at 17 months after injection. Fault permeability affects the pore fluid distribution across the fault, with a sealing fault favoring fault instability. Assessment of fault stability and earthquake probability associated with fluid injection using geomechanical modeling prior to the onset of seismic activity requires detailed site assessment of fault and in situ stress orientation, stress magnitudes, pore pressure prior to injection, and reservoir permeability structure.

References

ABAQUS (2014), *Abaqus User's Guide and Help Documentation*, Version 6.14, SIMULIA Company, Providence.

Abousleiman, Y., and S. Ekbote (2005), Solutions for the inclined borehole in a porothermoelastic transversely isotropic medium, *ASME.J. Appl. Mech.*, *72*, 102–114.

Ake, J., K. Mahrer, D. O'Connell, and L. Block (2005), Deep-injection and closely monitored induced seismicity at Paradox Valley, Colorado, *Bull. Seismol. Soc. Am.*, *95*, 664–683.

Altmann, J. B., T. M. Müller, B. I. R. Müller, M. R. Tingay, and O. Heidbach (2010), Poroelastic contribution to the reservoir stress path, *Int. J. Rock Mech. Min.*, *47*, 1104–1113.

Balkey, J. (1989), Ann McKnight (Paluxy) field, Smith County, Texas, in *Occurrence of Oil and Gas in Northeast Texas*, *East Texas Geol. Soc. Publ. Ser.*, 1989 ed., edited by P. W. Shoemaker, pp. 15–20, East Texas Geological Society, Tyler, Tex.

Barton, C. A., M. D. Zoback, and D. Moos (1995), Fluid flow along potentially active faults in crystalline rock, *Geology*, *23*(8), 683–686.

Bense, V. F., T. Gleeson, S. E. Loveless, O. Bour, and J. Scibek (2013), Fault zone hydrogeology, *Earth Sci. Rev.*, *127*, 171–192.

Berg, R. R., and A. F. Gangi (1999), Primary migration by oil-generation microfracturing in low-permeability source rocks: Application to the Austin chalk, Texas, *AAPG Bull.*, *83*, 727–756.

Boyd, R. F., and L. P. White (1989), Trawick (Travis Peak, James) field, Nacogdoches and Rusk counties, Texas, in *Occurrence of Oil and Gas in Northeast Texas*, *East Texas Geol. Soc. Publ. Ser.*, 1989 ed., edited by P. W. Shoemaker, pp. 191–196, East Texas Geological Society, Tyler, Tex.

Byerlee, J. D. (1978), Friction of rocks, *Pure Appl. Geophys.*, *116*, 615–626.

Caine, J. S., J. P. Evans, and C. B. Forster (1996), Fault zone architecture and permeability structure, *Geology*, *24*, 1025–1028.

Cappa, F., and J. Rutqvist (2011), Modeling of coupled deformation and permeability evolution during fault reactivation induced by deep underground injection of CO_2, *Int. J. Greenhouse Gas Control*, *5*, 336–346.

De Simone, S., V. Vilarrasa, J. Carrera, A. Alcolea, and P. Meier (2013), Thermal coupling may control mechanical stability of geothermal reservoirs during cold water injection, *Phys. Chem. Earth*, *64*, 117–126.

Dutton, S. P., and T. N. Diggs (1992), Evolution of porosity and permeability in the lower Cretaceous Travis Peak formation, east Texas, *AAPG Bull.*, *76*, 252–269.

Economides, M. J., and T. Martin (2007), *Modern Fracturing Enhancing Natural Gas Production*, ET Publishing, Houston, Tex.

Ellsworth, W. L. (2013), Injection-induced earthquakes, *Science*, *341*, 142–149.

Evans, K. F., A. Zappone, T. Kraft, N. Deichmann, and F. Moia (2012), A survey of the induced seismic responses to fluid injection in geothermal and CO_2 reservoirs in Europe, *Geothermics*, *41*, 30–54.

Ewing, T. (1990), *Tectonic Map of Texas*, Bureau of Economic Geology, The Univ. of Texas, Austin, Texas.

Finley, R. J., S. W. Speer, and R. J. Diecchio (1984), Geology and engineering characteristics of selected low-permeability gas sandstones: A national survey Bureau of Economic Geology Rep. Investigations 138, The University of Texas at Austin, Austin, Texas.

Frohlich, C. (2012), Two-year survey comparing earthquake activity and injection-well locations in the Barnett Shale, Texas, *Proc. Natl. Acad. Sci. U.S.A.*, *109*(13), 934–13,938.

Frohlich, C., and M. Brunt (2014), Two-year survey of earthquakes and injection/production wells in the Eagle Ford Shale, Texas, prior to the M_w4.8 20 October 2011 earthquake, *Earth Planet. Sci. Lett.*, *402*, 257–264.

Frohlich, C., and S. D. Davis (2002), *Texas Earthquakes*, 275 pp., Univ. Texas Press, Austin, Tex.

Frohlich, C., C. Hayward, B. Stump, and E. Potter (2011), The Dallas-Fort Worth earthquake sequence: October 2008 through May 2009, *Bull. Seismol. Soc. Am.*, *101*, 327–340.

Frohlich, C., W. Ellsworth, W. A. Brown, M. Brunt, J. Luetgert, T. MacDonald, and S. Walter (2014), The 17 May 2012 M4.8 earthquake near Timpson, East Texas: An event possibly triggered by fluid injection, *J. Geophys. Res. Solid Earth*, *119*, 581–593, doi:10.1002/2013JB010755.

Grubbs, E. L. (1953), Variations in porosity and permeability in the Wilcox Group of the Texas Upper Gulf Coast, *GCAGS Trans.*, *3*, 54–70.

Heidbach, O., M. Tingay, A. Barth, J. Reinecker, D. Kurfe, and B. Müller (2008), The World Stress Map database release 2008, doi:10.1594/GFZ. WSM.Rel2008.

Heidbach, O., M. Tingay, A. Barth, J. Reinecker, D. Kurfeß, and B. Müller (2010), Global crustal stress pattern based on the World Stress Map database release 2008, *Tectonophysics*, *482*(1–4), 3–15, doi:10.1016/j.tecto.2009.07.023.

Hornbach, M. J., et al. (2015), Causal factors for seismicity near Azle, Texas, *Nat. Commun.*, *6*, 11, doi:10.1038/ncomms7728.

Horton, S. (2012), Disposal of hydrofracking waste fluid by injection into subsurface aquifers triggers earthquake swarm in central Arkansas with potential for damaging earthquake, *Seismol. Res. Lett.*, *83*, 250–260.

Hsieh, P. A., and J. S. Bredehoeft (1981), A reservoir analysis of the Denver earthquakes—A case study of induced seismicity, *J. Geophys. Res.*, *86*, 903–920, doi:10.1029/JB086iB02p00903.

Ito, T., and M. Zoback (2000), Fracture permeability and in situ stress to 7 km depth in the KTB scientific drillhole, *Geophys. Res. Lett.*, *27*, 1045–1048, doi:10.1029/1999GL011068.

Jackson, M. P. A. (1982), *Fault Tectonics of the East Texas Basin*, Geol. Circular, 82-4, 31 pp., Bureau of Economic Geology, The Univ. of Texas at Austin, Austin, Tex.

Jha, B., and R. Juanes (2014), Coupled multiphase flow and poromechanics: A computational model of pore pressure effects on fault slip and earthquake triggering, *Water Resour. Res.*, *50*, 3776–3808, doi:10.1002/2013WR015175.

Keranen, K. M., H. M. Savage, G. A. Abers, and E. S. Cochran (2013), Potentially induced earthquakes in Oklahoma, USA: Links between wastewater injection and the M_W 5.7 earthquake sequence, *Geology*, *41*, 609–702.

Keranen, K. M., M. Weingarten, G. A. Abers, B. A. Bekins, and S. Ge (2014), Sharp increase in central Oklahoma seismicity since 2008 induced by massive wastewater injection, *Science*, *345*, 448–451.

Kim, W.-Y. (2013), Induced seismicity associated with fluid injection into a deep well in Youngstown, Ohio, *J. Geophys. Res. Solid Earth*, *118*, 3506–3518, doi:10.1002/jgrb.50247.

Kim, Y. S., and D. J. Sanderson (2005), The relationship between displacement and length of faults: A review, *Earth Sci. Rev.*, *68*, 317–334.

Konstantinovskaya, E., J. Rutqvist, and M. Malo (2014), CO_2 storage and potential fault instability in the St. Lawrence Lowlands sedimentary basin (Quebec, Canada): Insights from coupled reservoir-geomechanical modeling, *Int. J. Greenhouse Gas Control*, *22*, 88–110.

Laubach, S., and E. Monson (1988), Coring-induced fractures: Indicators of hydraulic fracture propagation in a naturally fractured reservoir Society of Petroleum Engineers, SPE-18164-MS.

Laubach, S. E., R. W. Baumgardner Jr., E. R. Monson, E. Hunt, and K. J. Meador (1988), Fracture detection in low-permeability reservoir sandstone: A comparison of BHTV and FMS logs to core Society of Petroleum Engineers, SPE-18119-MS.

Lucier, A., M. Zoback, N. Gupta, and T. S. Ramakrishnan (2006), Geomechanical aspects of CO_2 sequestration in a deep saline reservoir in the Ohio River Valley region, *Environ. Geosci.*, *13*, 85–103.

Luo, G., P. B. Flemings, M. R. Hudec, and M. A. Nikolinakou (2015), The role of pore fluid overpressure in the substrates of advancing salt sheets, ice glaciers, and critical-state wedges, *J. Geophys. Res. Solid Earth*, *120*, 87–105, doi:10.1002/2014JB011326.

Mancini, E., P. Aharon, D. A. Goddard, M. Horn, and R. Barnaby (2012), Basin analysis and petroleum system characterization and modeling Interior Salt Basins, Central and Eastern Gulf of Mexico, Part 3: Tectonic/Depositional History, Resource Assessment, AAPG Search and Discovery Article #10395.

McGarr, A. (2014), Maximum magnitude earthquakes induced by fluid injection, *J. Geophys. Res. Solid Earth*, *119*, 1008–1019, doi:10.1002/2013JB010597.

National Research Council (2013), *Induced Seismicity Potential in Energy Technologies*, Natl. Acad. Press, Washington, D. C.

Nicholson, C., and R. L. Wesson (1990), Earthquake hazard associated with deep well injection: A report to the U.S. Environmental Protection Agency U.S. Geol. Surv. Bull. 1951.

Nicholson, C., and R. L. Wesson (1992), Triggered earthquakes and deep well activities, *Pure Appl. Geophys.*, *139*, 561–578.

Parotidis, M., and S. A. Shapiro (2004), A statistical model for the seismicity rate of fluid-injection-induced earthquakes, *Geophys. Res. Lett.*, *31*, L17609, doi:10.1029/2004GL020421.

Peška, P., and M. D. Zoback (1995), Compressive and tensile failure of inclined well bores and determination of in situ stress and rock strength, *J. Geophys. Res.*, *100*, 12,791–12,811, doi:10.1029/95JB00319.

Peterson, R. E. (1989), Staged field experiment No. 2: Application of advanced geological, petrophysical and engineering technologies to evaluate and improve gas recovery from low permeability sandstone reservoirs—Volume 1 GRI report 89/0140, Gas Research Institute.

Plumb, R., S. Herron, and M. Olsen (1992), Composition and texture on compressive strength variations in the Travis Peak formation paper presented at SPE Annual Technical Conference and Exhibition, Society of Petroleum Engineers, SPE Paper 24758.

Plumb, R. A. (1989), Fracture patterns associated with incipient wellbore breakouts Paper presented at ISRM International Symposium on Rock at Great Depth, International Society for Rock Mechanics, Paris.

Pollard, N. (1989), Alabama Ferry (Glen Rose) field, Leon County, Texas, in *Occurrence of Oil and Gas in Northeast Texas*, *East Texas Geol. Soc. Publ. Ser.*, 1989 ed., edited by P. W. Shoemaker, pp. 1–14, East Texas Geological Society, Tyler, Tex.

Raleigh, C. B., J. H. Healy, and J. D. Bredehoeft (1972), Faulting and crustal stresses at Rangely, Colorado, *AGU Geophys. Monogr. Ser.*, *16*, 275–284.

Rinaldi, A. P., and J. Rutqvist (2013), Modeling of deep fracture zone opening and transient ground surface uplift at KB-502 CO_2 injection well, In Salah, Algeria, *Int. J. Greenhouse Gas Control*, *12*, 155–167.

Roeloffs, E., and R. Denlinger (2009), An axisymmetric coupled flow and deformation model for pore pressure caused by brine injection in Paradox valley, Colorado: Implications for the mechanisms of induced seismicity, Preliminary Report to the Bureau of Reclamation, *U.S. Geol. Surv.*, 31 pp.

Rudnicki, J. W. (1986), Fluid mass sources and point forces in linear elastic diffusive solids, *Mech. Mater.*, *5*, 383–393.

Rutqvist, J., J. Birkholzer, and C.-F. Tsang (2008), Coupled reservoir-geomechanical analysis of the potential for tensile and shear failure associated with CO_2 injection in multilayered reservoir-caprock systems, *Int. J. Rock Mech. Min. Sci.*, *45*(2), 132–143.

Schultz, R., V. Stern, and Y. J. Gu (2014), An investigation of seismicity clustered near the Cordel Field, west central Alberta, and its relation to a nearby disposal well, *J. Geophys. Res. Solid Earth*, *119*, 3410–3423.

Segall, P., and S. Lu (2015), Injection-induced seismicity: Poroelastic and earthquake nucleation effects, *J. Geophys. Res. Solid Earth*, *120*, 5082–5103, doi:10.1002/2015JB012060.

Shapiro, S. A., O. S. Kruger, and C. Dinske (2013), Probability of inducing given-magnitude earthquakes by perturbing finite volumes of rocks, *J. Geophys. Res. Solid Earth*, *118*, 3557–3575.

Texas Railroad Commission (2014). [Available at http://www.rrc.state.tx.us/about-us/resource-center/research/online-research-queries/ accessed Oct 1 2014.]

Texas Water Development Board (1972), *A Survey of the Subsurface Saline Water of Texas, Chemical Analyses of Saline Water*, *Report 157*, vol. 2, 378 pp., Texas Water Development Board, Austin, Tex.

Thayer, P. A. (1983), Relationship of porosity and permeability to petrology of the Madison Limestone in rock cores from three test wells in Montana and Wyoming.

Thiercelin, M., and R. Plumb (1994), A core-based prediction of lithologic stress contrasts in east Texas formations, *SPE Form. Eval.*, *9*, 251–258.

Vilarrasa, V., S. Olivella, J. Carrera, and J. Rutqvist (2014), Long term impacts of cold CO_2 injection on the caprock integrity, *Int. J. Greenhouse Gas Control*, *24*, 1–13.

Wang, H. (2000), *Theory of Linear Poroelasticity With Applications to Geomechanics and Hydrogeology*, Princeton Univ. Press, Princeton, N. J.

Wang, Y., and M. B. Dusseault (2003), A coupled conductive-convective thermo-poroelastic solution and implications for wellbore stability, *J. Petrol. Sci. Eng.*, *38*, 187–198.

Wells, D. L., and K. J. Coppersmith (1994), New empirical relationships among magnitude, rupture length, rupture width, rupture area, and surface displacement, *Bull. Seismol. Soc. Am.*, *84*, 974–1002.

Zoback, M. D. (2010), *Reservoir Geomechanics*, Cambridge Univ. Press, Cambridge, U. K., and New York.

Zoback, M. D., and H. P. Harjes (1997), Injection-induced earthquakes and crustal stress at 9 km depth at the KTB deep drilling site, Germany, *J. Geophys. Res.*, *102*, 477–18,491, doi:10.1029/96JB02814.

Zoback, M. D., D. Moos, L. Mastin, and R. N. Anderson (1985), Wellbore breakouts and in situ stress, *J. Geophys. Res.*, *90*, 5523–5530, doi:10.1029/JB090iB07p05523.